scientific reports

Check for updates

OPEN

Future projections of glacier mass change in High Mountain Asia using GRACE and climatemodel data

Jaydeo K. Dharpure[1✉], Ian M. Howat[1,2] & Akansha Patel[3]

High Mountain Asia (HMA) is a critical region for global water resources, where glacier monitoring, modeling, and prediction are essential to understanding the impacts of climate change on water availability and related hazards. This study examined glacier mass change in HMA using terrestrial water storage anomaly data from gravity recovery and climate experiment (GRACE) and GRACE Follow-On. Our results reveal significant glacier mass loss of − 13.9 ± 3.6 Gt/yr between 2002/03 and 2022/23, with pronounced spatial variability across subregions. Eastern Kunlun shows the highest mass gain (1.1 ± 0.2 Gt/yr), while the West Tien Shan experiences the most rapid mass loss (–1.9 ± 0.4 Gt/yr). For future projections, we employed a generalized additive model driven by climate and radiative flux variables from the Inter-Sectoral Impact Model Intercomparison Project under low- (SSP126) and high-emission (SSP585) scenarios. The results indicate continued glacier mass decline, with the steepest reductions under SSP585 (− 19.5 ± 11.3 Gt/yr) compared to SSP126 (− 2.3 ± 0.3 Gt/yr). These changes occurred due to variation in climatic and radiative fluxes in both past and future projections. Overall, our study enhances understanding of cryospheric change in HMA, providing critical insights for future research, climate adaptation, and water resource management.

Keywords Climate change, Glacier mass change, GRACE satellites, Predictions

High Mountain Asia (HMA) is a critical region within the Earth's cryosphere, hosting extensive glacier systems that serve as vital freshwater reservoirs, supporting millions of people[1]. Often called the "water towers of Asia," these glaciers provide essential water resources for some of the world's most densely populated regions[2,3], significantly influence regional hydrology and contributing to global climate regulation[4,5]. In upstream regions, glacial meltwater is indispensable for hydropower generation, renewable energy, and large-scale irrigation systems[6,7]. In recent decades, HMA has experienced accelerated glacier mass loss driven by rising temperatures, altered precipitation patterns, and increasing climatic variability[8,9]. This rapid decline poses serious challenges for long-term water security, ecosystem resilience, and downstream hydrological stability[10,11].

Traditional approaches for estimating glacier mass change, such as in situ observations[12,13], provide highly accurate point-scale measurements and serve as critical benchmarks for validating model-based estimates. However, these methods are logistically challenging and often infeasible in remote and high-altitude regions of the Himalaya[1]. Geodetic techniques[14–16], extend spatial coverage but are limited by low temporal resolution, restricting their ability to capture seasonal or short-term variability. Optical and radar remote sensing methods[17–19], offer broader spatial and temporal coverage, enabling large-scale assessments across glacierized areas, yet they remain affected by cloud contamination, radar signal backscatters, and uncertainties in debris-covered or shadowed regions. Collectively, these limitations highlight the need for robust, large-scale monitoring frameworks that can provide spatially continuous and temporally consistent assessments of long-term glacier mass changes across the HMA region.

Satellite gravimetry, particularly data from the gravity recovery and climate experiment (GRACE) and its successor GRACE Follow-On (GRACE-FO), has transformed the ability to monitor regional glacier mass change (GMC) by detecting variation in terrestrial water storage[20–22]. However, a major challenge is the 11-month gap between the missions, which interrupts the continuity of long-term glacier mass monitoring[23]. To address this, several statistical[24,25], machine learning[26,27], and deep learning [[27,28,29],] models have been applied, but their performance varies across climatic conditions, particularly between humid and arid regions[30]. Many studies demonstrate that the MissForest machine learning algorithm provides robust gap-filling capabilities for both short- and long-term gaps in hydrological datasets due to its iterative imputation and ability to capture nonlinear

[1]Byrd Polar and Climate Research Center, The Ohio State University, Columbus 43210, USA. [2]School of Earth Sciences, The Ohio State University, Columbus 43210, USA. [3]Texas A&M AgriLife, Blackland Research and Extension Center, Temple, TX 76502, USA. ✉email: jaydharpure2007@gmail.com

hydroclimatic variability[29,30]. In particular[32], applied MissForest to fill gaps in gravimetry data using various hydro-climatic variables and reported that it outperformed other approaches. Therefore, gap filling in gravimetry data remains challenging at large spatial scales and requires robust validation for accuracy assessment.

Numerous studies have quantified glacier mass loss across HMA, revealing pronounced spatial heterogeneity[8,33,34]. For example[35], reported substantial losses in the Nyainqentanglha range and gains in the Kunlun region between 2000 and 2016. Similarly[36], highlighted contrasting mass balance patterns, noting positive trends in the eastern Karakoram and West Kunlun, but negative trends in adjacent areas such as Jammu & Kashmir and the Himalayas, reflecting the highly heterogeneous climate influence across HMA. Further[37], reported significant mass losses in the Nyainqentanglha Mountains and Eastern Himalayas and slight gains in the Karakoram and Western Kunlun, attributing these patterns primarily to net radiation and providing key insights into glacier–climate interactions. Despite these findings, GRACE-based studies have largely focused on glacier mass trends while rarely examining the relative contributions of radiative fluxes, which remain critical yet underexplored drivers of melt variability. Identifying how these radiative and climatic variables jointly influence GMC across spatial and seasonal scales remains an important research gap. Recent advancements in machine learning have provided new opportunities to explore these complex relationships and quantify the contribution of individual climatic variables to observed GMC[38,39].

Future projections of GMC in HMA consistently indicate continued mass loss under various climate scenarios[40–42]. Most models rely on general circulation models (GCMs) for climate inputs, which are limited by coarse spatial resolution and uncertainties in representing small-scale processes, restricting their accuracy for regional projections. The Inter-Sectoral Impact Model Intercomparison Project Phase 3b (ISIMIP3b) addresses these limitations by providing harmonized, bias-adjusted, high-resolution datasets for historical and future simulations under standardized scenarios[43,44]. Bias-corrected ISIMIP3b daily forcing has been used to project global glacier mass balance from 1851 to 2100 across various shared socioeconomic pathways (SSPs) and to assess equilibrium volume and area under stabilized temperatures[45], and these datasets have also proven effective in projecting extreme events[46–49]. Generalized additive models (GAMs) have become increasingly popular for such projections because they offer a flexible, semi-parametric framework capable of capturing nonlinear relationships between environmental variables while maintaining interpretability[50,51]. This balance of flexibility and transparency makes GAMs a robust choice for projecting future hydrological variables[25].

In this study, we analyze GMC across HMA and its 15 sub-regions over the past two decades using GRACE and GRACE-FO satellite gravimetry. The novelty of this work lies in several key aspects:

- **GRACE and GRACE-FO gap filling using machine learning**: We employ the MissForest algorithm to bridge data gaps between GRACE and GRACE-FO, ensuring continuous and consistent monitoring of GMC at both regional and sub-regional scales.
- **Integration of climatic and radiative flux variables**: In addition to temperature and precipitation, we incorporate specific humidity, incoming shortwave, and longwave radiation to quantify their independent and combined influence on GMC.
- **Non-parametric GMC modeling using GAM**: We employ a GAM to capture nonlinear and physically interpretable relationships between GMC and its climatic–radiative drivers.
- **Scenario-based future projections**: Using bias-corrected ISIMIP3b climate data under low- (SSP126) and high-emission (SSP585) scenarios, we provide forward-looking insights into potential glacier mass loss through the end of the 21st century.

Overall, this study integrates satellite gravimetry, machine learning techniques, and future climate scenarios analysis to advance understanding of glacier-climate interactions and highlight the potential risks posed by continued mass loss under high-emission pathways.

Results

Performance evaluation of missforest based gap filling

The MissForest method is used to fill a 33-month data gap in GRACE and GRACE-FO observations from April 2002 to December 2023. Model performance is evaluated by randomly splitting the data into 70% for training and 30% for testing. Predicted terrestrial water storage anomaly (TWSA) values show strong agreement with observations, achieving an R^2 of 0.92 and a root mean square error (RMSE) of 22.7 mm. A comparison with global land data assimilation system (GLDAS) catchment land surface model (CLSM)-derived TWSA further yields an R^2 of 0.83 and an RMSE of 32.5 mm, confirming the reliability of the trained MissForest model. Dharpure et al. (2025a) [32] applied the same approach in the Indus River basin and found that MissForest outperformed five existing gap-filling methods, including seasonal-trend decomposition procedure based on Loess (STL). While STL has been shown effective in reconstructing TWSA[52,53], it may miss signal variations linked to hydroclimatic drivers. Finally, the trained MissForest model was applied to reconstruct TWSA for all months with missing data between the GRACE and GRACE-FO missions (Fig. S1).

Current trend in glacier mass change (2002–2023)

Glacier mass change

The GMC analysis across the HMA and its subregions reveals spatially variable mass changes from 2002 to 2023. The overall mass change for the HMA is estimated at -13.9 ± 3.6 Gt/yr, equivalent to an average loss of -9.0 ± 2.4 mm/yr over the region (Table 1). Subregional trends highlight pronounced variability: the CH and EH show mass losses of -1.3 ± 0.4 Gt/yr and -1.0 ± 0.2 Gt/yr, respectively, with corresponding thinning rates over glacierized areas reaching -0.19 ± 0.8 mm/yr and -0.17 ± 0.5 mm/yr. In contrast, the EK exhibits a mass gain of 1.1 ± 0.2 Gt/yr, suggesting a localized glacier mass gain and indicating that the "Karakoram anomaly" may be

Region	Min (mm)	Max (mm)	Mean (mm)	Mass change (Gt/yr) ± Error	Over grid area (mm/yr) ± Error	Over glacier area (mm/yr) ± Error
Central Himalaya (CH)	−318.6	77.0	−113.3	**-1.3 ± 0.4**	**-19.5 ± 5.6**	**-0.19 ± 0.8**
Eastern Himalaya (EH)	−255.0	44.9	−98.2	**-1.0 ± 0.2**	**-15.0 ± 2.6**	**-0.17 ± 0.5**
East Kunlun (EK)	−34.4	177.1	76.6	**1.1 ± 0.2**	**11.2 ± 2.6**	**0.35 ± 0.8**
East Tien Shan (ET)	−407.2	54.5	−132.8	**-1.4 ± 0.2**	**-21.1 ± 4.2**	**-0.47 ± 0.7**
Hengduan Shan (HS)	−259.4	94.6	−106.8	**-1.6 ± 0.4**	**-15.7 ± 4.4**	**-0.41 ± 0.6**
Hindu Kush (HK)	−204.0	50.7	−51.4	**-0.6 ± 0.4**	**-9.4 ± 6.6**	**-0.2 ± 2.2**
Hissar Alay (HA)	−241.7	54.1	−68.3	**-0.6 ± 0.2**	**-12.8 ± 5.4**	**-0.32 ± 3.0**
Inner Tibet (IT)	−24.8	41.9	7.3	0.3 ± 0.8	1.2 ± 3.4	0.04 ± 0.4
Karakoram (KK)	−121.9	24.8	−32.4	**-0.6 ± 0.4**	**-5.4 ± 3.2**	**-0.03 ± 0.2**
Pamir (PM)	−230.0	53.7	−61.3	**-1.4 ± 0.6**	**-12.4 ± 5.6**	**-0.14 ± 0.6**
Qilian Shan (QS)	−29.3	14.8	−7.0	**-0.1 ± 0.2**	**-1.2 ± 2.4**	**-0.05 ± 1.4**
Southeast Tibet (ST)	−232.8	34.2	−76.3	**-1.3 ± 0.4**	**-12.2 ± 4.0**	**-0.29 ± 0.8**
Western Himalaya (WH)	−299.0	39.6	−81.6	**-1.8 ± 0.6**	**-13.0 ± 4.0**	**-0.22 ± 0.6**
West Kunlun (WK)	−31.0	46.6	15.0	**0.2 ± 0.2**	**2.6 ± 2.6**	**0.02 ± 0.4**
West Tien Shan (WT)	−229.9	29.5	−77.3	**-1.9 ± 0.4**	**-12.2 ± 3.0**	**-0.21 ± 0.4**
High Mountain Asia (HMA)	−173.5	22.9	−53.9	**-13.9 ± 3.6**	**-9.0 ± 2.4**	**-0.14 ± 0.2**

Table 1. Statistical summaries and trends (Sen's slope) over glacier grids and glacier areas across 15 subregions and the HMA, covering 21 hydrological years from 2002/03 to 2022/23. Bold values indicate statistically significant mass change ($p < 0.05$). Uncertainty is reported as ± 2 standard deviations (2σ).

shifting eastward, as the KK itself shows a mass loss of − 0.6 ± 0.4 Gt/yr. The fastest losses are observed in the WT and WH, exceeding − 1.8 Gt/yr. All trends are statistically significant at $p < 0.05$, except for the IT.

Spatial distribution of GMC rates ($p < 0.05$) across glacier grids reveals heterogeneous patterns with pronounced regional variability (Fig. 1). Strong negative mass changes are observed in the WH, WT, HK, and CH, indicating substantial thinning. In contrast, localized positive changes in the EK and parts of the IT suggest mass gains consistent with the shifting influence of the "Karakoram anomaly." The EH and HS also show considerable losses, while relatively moderate changes are found in the QS. Most of the HMA has exhibited consistent negative mass change since 2005/06, with ET and WT following from 2007/08. In contrast, HK, KK, HA, and PM regions show heterogeneous annual variations before stabilizing into consistent losses by 2010/11. Overall, these results highlight the spatially variable glacier response to climatic and hydrological drivers across HMA, with most subregions exhibiting significant negative mass trends.

Distribution of hydroclimatic variables

The long-term Sen's slope of six hydroclimatic variables such as precipitation (P), air temperature (T_a), land surface temperature (T_s), specific humidity (SH), incoming shortwave (SWI), and incoming longwave (LWI) radiation across the HMA and its subregions is summarized in Table S1. Trends in P show strong spatial heterogeneity, with declines in EH, WT, and HK, while localized increases occur in WH, WK, and QS. Temperature trends, by contrast, are uniformly positive, with T_a rising at ~ 0.02–0.06 °C/yr and T_s following a similar pattern, confirming a robust warming signal across the region. SH shows modest but consistent increases (~ 0.01–0.02 g/kg/yr), reflecting a gradual intensification of atmospheric moisture supply that may influence snow and precipitation phase transitions[54]. Radiation trends exhibit a dipole pattern: SWI decreases across most subregions (e.g., EH, and CH), likely linked to enhanced cloud cover and aerosol loading, while LWI shows widespread increases, strongest in WK (+ 0.23 ± 0.16 W/m^2/yr) and ST (+ 0.22 ± 0.24 W/m^2/yr). Rising LWI contributes additional glacier surface energy input, enhancing melt even under reduced shortwave fluxes[55]. At the HMA-wide scale, precipitation changes are negligible (+ 1.06 ± 1.78 mm/yr), but the region shows clear warming (+ 0.04 ± 0.03 °C/yr for T_a; +0.04 ± 0.04 °C/yr for T_s), increasing LWI (+ 0.17 ± 0.11 W/m^2/yr), and declining SWI (− 0.15 ± 0.10 W/m^2/yr). Collectively, these results indicate that while precipitation remains spatially heterogeneous, consistent warming and radiative flux changes are the primary drivers of glacier mass loss and altered hydrological regimes in the HMA.

Spatial patterns of long-term trends (Sen's slope) in six hydroclimatic variables are analyzed across the HMA from 2002/03 to 2022/23 (Fig. 2). These variables are systematically monitored to capture their regional trends and anomalies, forming the basis for understanding the linkages between climatic drivers and glacier mass changes. Precipitation is spatially heterogeneous, with pronounced declines in parts of the eastern and western Himalayas, while increases are observed in some northern regions. The estimates of T_a display widespread warming across HMA, with stronger increases in the central and western regions, ranging from − 0.03 to 0.11 °C/yr. A similar trend in T_s is observed, revealing consistent warming across most of HMA, particularly in the western and central subregions, with changes between − 0.05 and 0.12 °C/yr. SH generally increases throughout the region, with the highest positive trends concentrated in the WH. Rising T_a and SH suggest increased atmospheric moisture content. However, localized decreases in SH are observed in parts of the eastern HMA, highlighting regional variability. SWI generally decreases over the southern and central HMA, whereas slight positive trends appear in the northern areas. In contrast, LWI shows an overall increase, especially in

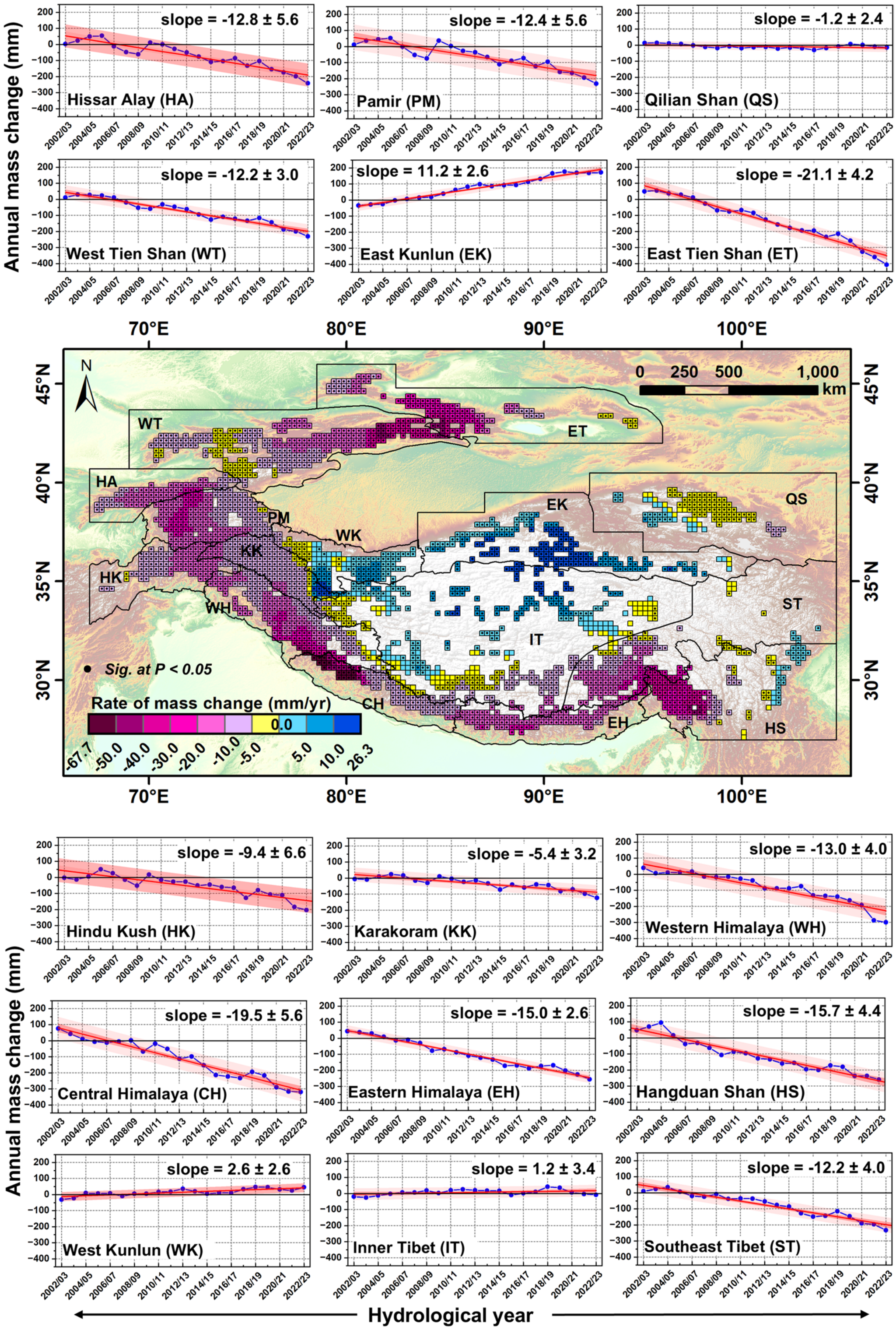

Fig. 1. Spatial distribution of glacier mass change rates across the HMA and mean annual temporal patterns of mass change in 15 sub-regions from the 2002/03 to 2022/23 hydrological years (October–September). The red curve represents the best-fit linear trend, with the shaded red area indicates the 95% confidence interval. The study area map was created using ArcGIS 10.8 (https://www.esri.com), and the temporal plots were generated using OriginPro 2025 (https://www.originlab.com).

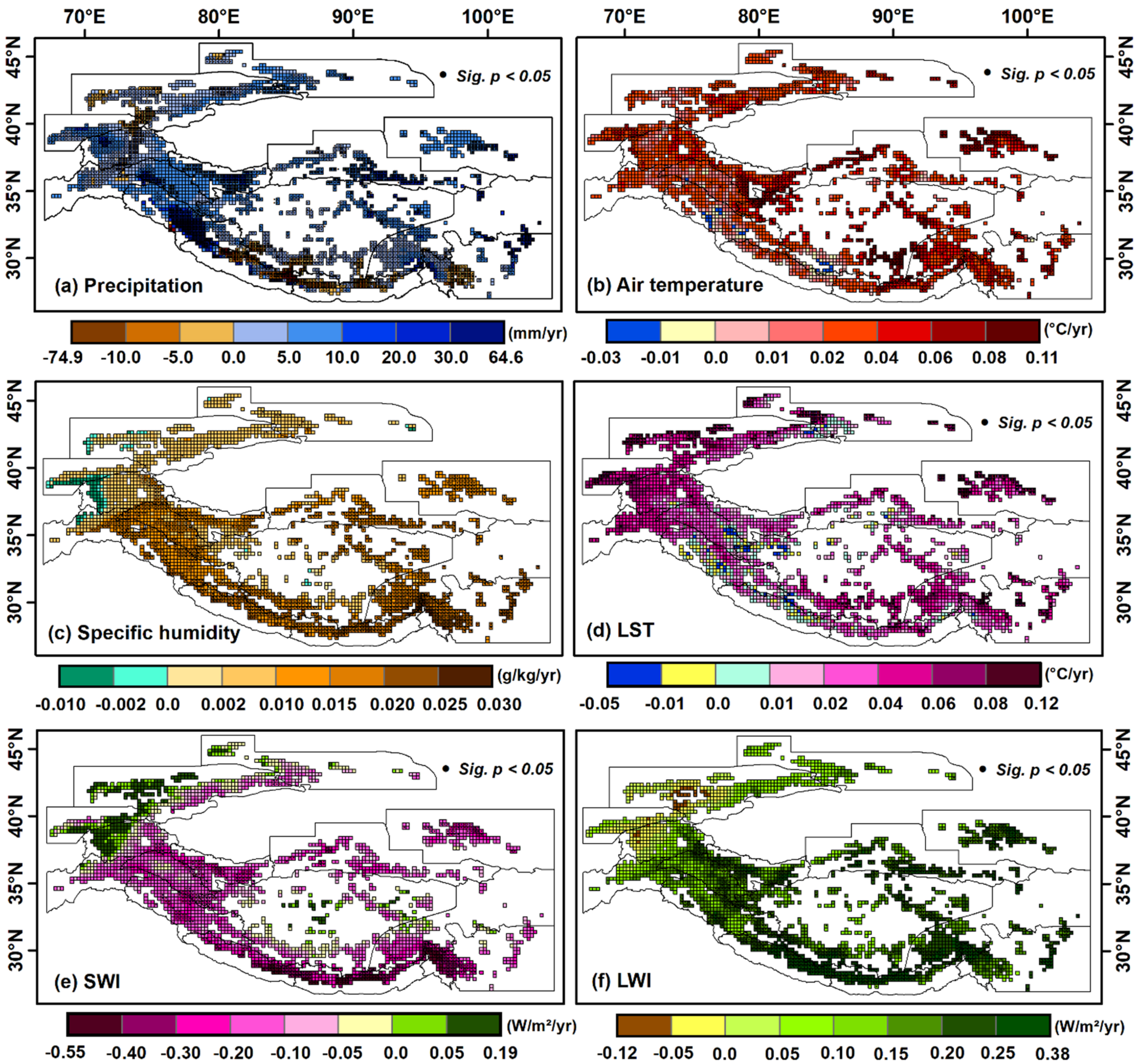

Fig. 2. Spatial trends of climatic variables and radiative fluxes across HMA (2002/03–2022/23): **(a)** Precipitation, **(b)** Air temperature, **(c)** Specific humidity, **(d)** Land surface temperature (LST), **(e)** incoming shortwave radiation (SWI), and **(f)** incoming longwave radiation (LWI).

northern and western HMA. Overall, these results highlight substantial spatial heterogeneity in hydroclimatic trends across HMA, reflecting complex interactions between climatic drivers and regional topography.

Projecting of future glacier mass change

Input variables

Historical and projected temporal variability in five input variables is analyzed (Fig. 3). P increases during the reference period (1.06 mm/yr) and both future scenarios, with a smaller increase under SSP126 (0.67 mm/yr) and a larger one under SSP585 (3.10 mm/yr). Reference and projected T_a and SH also increase, except for SH under SSP126, which showed no trend. The observed rise in P and T_a suggests a shift from snowfall to rainfall at higher elevations. Under warmer conditions, P is more likely to fall as rain rather than snow, lowering the rain–snow transition altitude. This shift could enhance snow accumulation in some regions but simultaneously accelerate ablation, leading to greater glacier mass loss. The increase in SH further indicates higher atmospheric moisture, which may intensify P; however, the predominance of rain instead of snow under warming conditions could amplify glacier melting and compound mass loss.

The SWI and LWI radiation show opposing patterns. During the reference period, LWI increases (0.17 W/m^2/yr) while SWI decreases (0.15 W/m^2/yr), nearly offsetting each other. In future scenarios, LWI continues to increase under both SSP126 and SSP585, whereas SWI increases under SSP126 but decreases under SSP585, consistent with the reference period pattern. These radiative trends suggest that increasing LWI, driven by

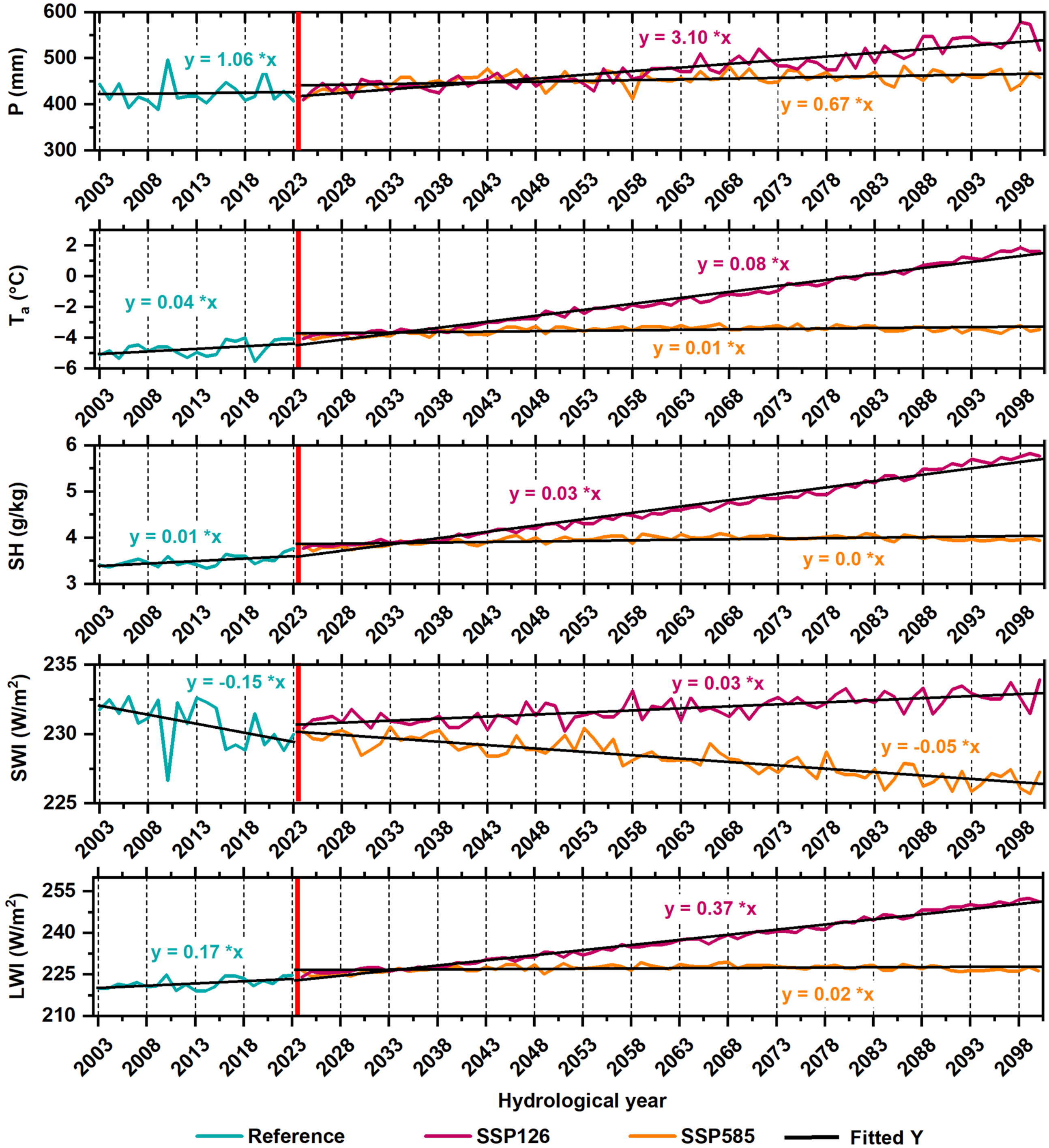

Fig. 3. Annual variability of input variables during the reference period (2002/03–2022/23) and future scenarios (SSP126 and SSP585, 2023/24–2099/2100) are analyzed based on the hydrological year (October to September).

atmospheric warming and higher humidity, will likely intensify glacier surface melting across all scenarios. The contrasting behavior of SWI under different scenarios highlights the potential variability in energy input to glacier surfaces, with SSP585 posing a higher risk of accelerated glacier mass loss due to the compounded effects of rising LWI and reduced SWI.

Overall, P patterns shift toward more rainfall under warmer conditions. The consistent increase in LWI and reduced SWI under SSP585 are likely to further accelerate surface melting. These findings underscore the heightened vulnerability of glaciers under high-emission scenarios and the urgent need for emission mitigation to manage future hydrological and cryospheric changes.

Changes in climatic variables and radiative fluxes
Projected changes in key climate variables and radiative fluxes under two emission scenarios (SSP126 in green and SSP585 in red) are shown across three future periods (Early, Mid, and Late) relative to the reference period (2002–2023) (Fig. S2). P increases under both scenarios but rises more sharply under SSP585, with late century increases of 8.4% (SSP126) and 22.7% (SSP585). T_a shows consistent increases across all periods, with late century warming of 1.0–1.3 °C (SSP126) and 4.5–6.6 °C (SSP585). SH follows this pattern, with greater increases under SSP585. Similarly, LWI rises more steeply under SSP585, while SWI exhibits opposing trends, increasing under SSP126 but decreasing under SSP585. These results highlight the stronger impacts of high-emission pathways, with the late century showing the most dramatic changes across all variables. The contrasting responses between SSP126 and SSP585 emphasize the importance of adopting low-emission pathways to mitigate long-term climate and cryospheric impacts.

Future glacier mass change
For model development, various combinations of input variables, including climatic factors, radiative fluxes, and their combined effects—were tested in the region (Fig. S3). Three models (M1–M3) were trained and validated using a random split of 70% and 30% of the data, respectively. Among them, M3 (inputs: P, Ta, SH, SWI, and LWI) achieved the best performance with an R^2 of 0.94 and an RMSE of 22.8 mm. In comparison, M1 (inputs: P, Ta, and SH) ranked second, while M2 (inputs: SWI, and LWI) performed the weakest over testing data. M3 model's ability to integrate both climatic and radiative flux variables enabled it to capture the observed peaks and troughs of GMC more accurately, underscoring its strength in representing the complex drivers of mass change dynamics in the HMA. Therefore, M3 was selected as the optimal model for predicting future mass changes.

Figure 4 presents the projected GMC in HMA for the reference period (2002/03–2022/23) and the future period (2023/24–2099/2100) under SSP126 and SSP585 scenarios. The reference period indicates substantial ongoing mass loss at 13.9 ± 3.6 Gt/yr. Future projections highlight contrasting trajectories between the low-emission (SSP126) and high-emission (SSP585) pathways. Under SSP126, the rate of mass loss slows considerably (− 5.2 ± 1.9 to − 2.7 ± 1.1 Gt/yr), with minimal residual loss expected toward the late 21st century, suggesting the potential benefits of strong mitigation in reducing cryospheric decline. In contrast, SSP585 projects accelerated glacier mass loss, with rates increasing from − 14.0 ± 6.1 Gt/yr in the early century to − 18.3 ± 11.0 Gt/yr by mid-century and further steepening to − 24.5 ± 15.3 Gt/yr by the late century. By 2049/50, SSP585 exhibits nearly three times higher loss than SSP126, followed by a significantly sharper decline thereafter. In the late century, SSP585 projects significant mass loss, while SSP126 shows a slightly positive mass balance (0.8 ± 1.2 Gt/yr). Overall, both scenarios show declining trends, with SSP585 reaching the highest loss rate (− 19.5 ± 11.3 Gt/yr) compared to a much slower decline under SSP126 (− 2.3 ± 0.3 Gt/yr). The shaded regions represent 95%

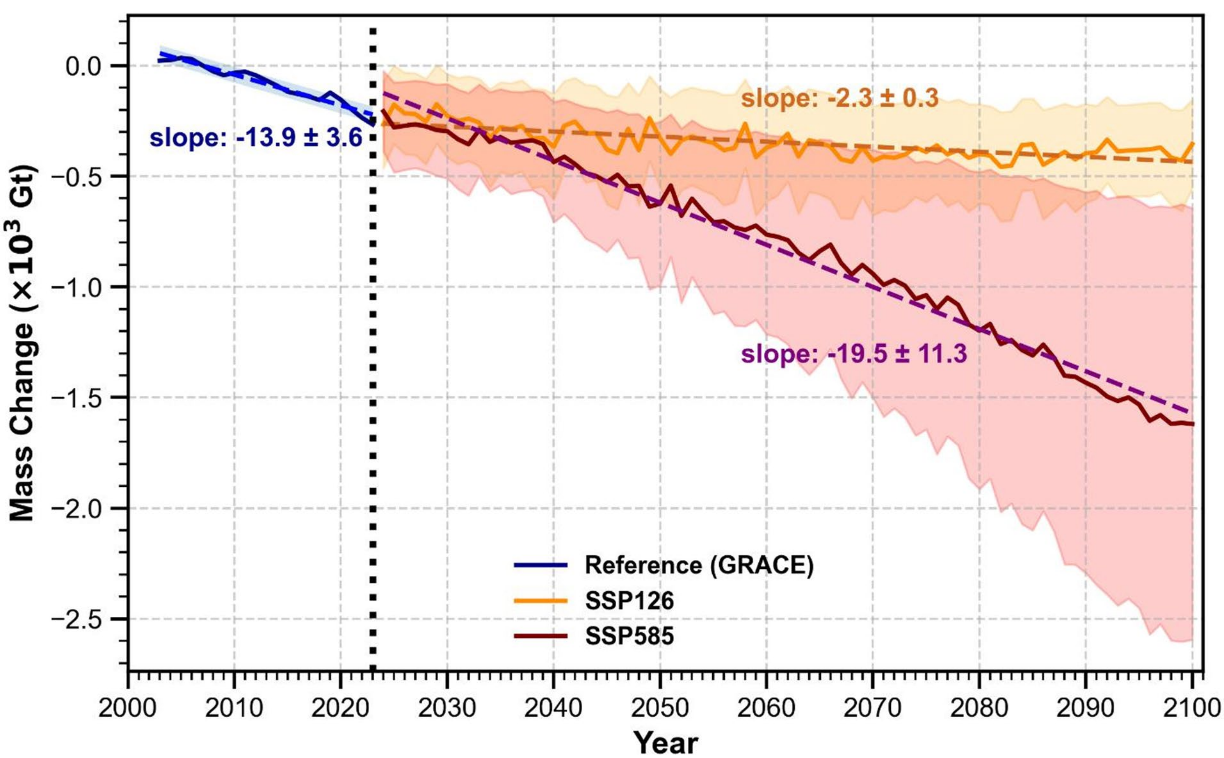

Fig. 4. Observed and projected glacier mass change (GMC) over the HMA. Solid lines represent the reference GRACE/GRACE-FO observations (2002/03–2022/23) and future projections under SSP126 and SSP585 (2023/24–2099/2100). Shaded regions denote uncertainty (± 2σ). Dashed lines indicate linear trends for each period.

confidence intervals, highlighting the uncertainty in projections. These results highlight the potential differences in glacier mass loss between the two scenarios, with more severe mass loss occurring under the SSP585 scenario, indicating greater warming and associated environmental changes in the future.

Discussion

This study advances previous GRACE-based GMC assessments in several important ways. First, applying the MissForest model to bridge GRACE and GRACE-FO data gaps improves temporal continuity and robustness, without relying on strong parametric assumptions. Second, it explicitly integrates climatic and radiative flux variables, enabling a more complete and physically grounded assessment of glacier–climate interactions than studies that primarily focused on trend estimation using GRACE or geodetic approaches and often considered climate drivers only implicitly. Third, the use of a non-parametric GAM allows the quantification of nonlinear yet interpretable relationships between GMC and its climatic–radiative drivers. Finally, coupling this framework with bias-corrected ISIMIP3b climate projections provides scenario-based insights into future GMC evolution, extending GRACE-based analyses from retrospective assessment to forward-looking risk evaluation.

Overall GMC across HMA decreased at a rate of 13.9 ± 3.6 Gt/yr during 2002–2023, indicating persistent mass loss over the past two decades. This estimate is broadly consistent with previous studies, while exhibiting notable differences attributable to variations in datasets, methodologies, and analysis periods (Table 2). Geodetic assessments have reported higher loss rates, including 16.3 ± 3.5 Gt/yr for 2000–2016[35] and 19.0 ± 2.5 Gt/yr for 2000–2018[56]. Similarly, GRACE-based studies have reported even higher loss rates such as 28.0 ± 6 Gt/yr for 2003–2019[8] and 22.2 ± 2.0 Gt/yr for 2002–2016[37]. In contrast, our results are closer to those of[57], who reported a loss rate of 17.7 ± 11.3 Gt/yr during 2002–2016 using GRACE observation. The comparatively lower estimate in this study likely reflects the longer analysis period extending into recent years, as well as differences in glacier delineation, and methodological approaches.

At the regional scale, spatial heterogeneity is evident. The Karakoram shows a decreasing trend, while the EK demonstrates positive mass change, consistent with Sakai and Fujita (2017b) [36]. Guan et al. (2022) [58] attributed changes in the WK region to the higher concentration of surge-type glaciers, while Zhang et al. (2020) [59] reported advancing glaciers in the Inner Tibetan Plateau, and Zhou et al. (2025) [22] reported a westward shift of the Karakoram anomaly using GRACE data. Our results exhibited a persistent negative trend since 2007/08, in agreement with Wang et al. (2021a) [8] the Karakoram anomaly persisted over the, who reported a widespread decline across the Himalayas, Tien Shan, and Pamir-Karakoram regions.

These findings are consistent with previous glacier mass balance studies in HMA, which highlight heterogeneous glacier responses driven by regional climatic and topographic variability[11,33,60,61]. Western regions such as CH, HS, and the ET–WT junction exhibit pronounced mass loss due to rising temperatures, reduced snowfall, and shifts in precipitation regimes[35,62,63], whereas southern EK and IT show localized mass gains likely associated with increased precipitation and snowfall influenced by westerly circulation and rain-shadow effects[22,64,65]. A warming trend is evident across HMA, with positive trends in both air temperature and SH indicating enhanced atmospheric moisture, although localized SH declines in eastern regions highlight strong regional variability. Concurrent decreases in SWI and increases in LWI reflect greater cloud cover and higher atmospheric emissivity associated with increased humidity[66–68]. Enhanced humidity and cloudiness increase downward LWI, which suppresses nighttime radiative cooling and raises net surface energy, thereby sustaining melt during nighttime even when daytime solar input is reduced. This longwave-driven energy feedback provides a physical mechanism linking atmospheric moisture to enhanced glacier melt and helps explain the observed mass changes across HMA, consistent with similar radiative shifts reported over the Tibetan Plateau and Himalayas[69]. These interactions between climate variability, energy fluxes, and atmospheric moisture underscore the complexity of glacier response and emphasize the need to incorporate both climatic and radiative processes when assessing glacier mass change trends.

The glacier mass loss observed across HMA mirrors global patterns reported for other major mountain systems, including the Andes, Alps, and Rocky Mountains, where sustained warming has driven widespread glacier retreat and declining meltwater contributions[70–72]. Studies show that glaciers worldwide are experiencing accelerated shrinkage, driven by rising temperatures and changes in precipitation patterns[73–75]. In the European

Study	Dataset	Method	Period	GMC (Gt/yr)	% difference
This study	GRACE, GRACE-FO	GRACE-based	2002–2023	−13.9 ± 3.6	-
Ciracì et al. (2020) [33]	GRACE, GRACE-FO	GRACE-based	2002–2019	−28.8 ± 12.0	−107.2
Wang et al. (2021) [8]	GRACE, GRACE-FO	GRACE-based	2003–2019	−28.0 ± 6.0	−101.4
Wouters et al. (2019) [57]	GRACE	GRACE-based	2002–2016	−17.7 ± 11.3	−27.3
Xiang et al. (2021) [37]	GRACE	GRACE-based	2002–2016	−22.2 ± 2.0	−59.7
Brun et al. (2017) [35]	ASTER	Geodetic	2000–2016	−16.3 ± 3.5	−17.3
Shean et al. (2020) [56]	ASTER	Geodetic	2000–2018	−19.0 ± 2.5	−36.7
Wang et al. (2021) [8]	ICESat, ICESat-2, SRTM	Geodetic	2003–2019	−27.7 ± 9.6	−99.3
Hugonnet et al. (2021) [140]	ASTER	Geodetic	2000–2019	−21.1 ± 1.7	−51.8
Fan et al. (2022) [80]	ICESat-2, NASADEM	Geodetic	2000–2021	−17.5 ± 11.4	−25.9

Table 2. Comparison of glacier mass change (GMC) estimates from this study and previous GRACE-based and geodetic studies. Percentage differences are calculated relative to the GMC estimated in this study.

Alps, unprecedented mass-balance losses have been documented, while the Andes have exhibited rapid retreat rates far exceeding historical norms[76–78]. These consistent global signals highlight the urgency of integrating glacier change into global and regional water resource adaptation strategies.

Direct validation of GMC against independent datasets such as ICESat-2 or regional geodetic mass balance estimates, remains challenging at the HMA scale due to differences in spatial resolution, temporal sampling, and glacier coverage[79,80]. Although ICESat-2 provides high-precision elevation change estimates but remains spatially discontinuous and temporally limited for regional-scale integration[81]. Similarly, geodetic datasets often focus on selected glacierized areas rather than providing comprehensive regional coverage[82,83]. However, the consistency of our results with multiple independent estimates supports the robustness of the GRACE-based signal.

For estimating uncertainty in GMC predictions, we used GRACE and GLDAS TWSA over the HMA. GRACE TWSA contains inherent uncertainties arising from measurement errors, data processing algorithms, and post-processing methods. To reduce biases, we utilized the ensemble mean of three mascon solutions (CSR, GSFC, and JPL) as recommended in previous studies[84,85]. GLDAS-derived TWSA is generated using a combination of field and satellite-based observations with advanced land surface modeling[86], but it does not account for anthropogenic factors or surface water bodies (e.g., lakes, ponds, rivers), introducing uncertainties in mass change estimates. We assumed surface water contributions to be negligible compared to glacier mass changes, consistent with earlier studies[22,34,87]. Additional uncertainty arises from decomposing GRACE signals into trends and residuals; the MissForest model was trained on detrended data with trends reintroduced after prediction, which could introduce uncertainties[28]. Moreover, GRACE TWSA trends can be influenced by anthropogenic activities not represented in reanalysis datasets[88,89]. Finally, our model did not incorporate time-lagged data during training, potentially influencing TWSA estimates for subsequent months. While the MissForest algorithm is computationally intensive, it can be optimized using parallel processing to improve efficiency[90].

A limitation of this study is the challenge in distinguishing glacier mass changes from other influencing hydrological variables within the GRACE TWSA grid (0.25° resolution). While we focused on grids encompassing glacier boundaries provided by RGI-7 over the HMA, some grid cells may have minimal glacier coverage, with mass changes predominantly driven by other hydrological factors. This variability introduces uncertainties, as glacier contributions within individual grids may not fully represent regional mass changes. Several authors have highlighted this issue in GMC analyses[91,92]. Despite these challenges, calculating regional glacier mass changes at fine spatial scales remains complex. To address this, we incorporate additional climatic and radiative forcings into our model to better capture the drivers of glacier mass changes and reduce potential biases. Future work could benefit from integrating additional geophysical corrections and leveraging advanced downscaling techniques to refine grid-based assessments of glacier contributions.

Projected glacier mass changes under different SSP scenarios have direct implications for water security, agriculture, and hazard management. Under high-emission pathways (SSP585), glacier mass loss is projected to accelerate substantially, with an aggregate loss rate of -19.5 ± 11.3 Gt/yr, indicating not only strong mass depletion but also large uncertainty in the magnitude of future losses. This enhanced melt is expected to intensify short-term flood risks, including glacier lake outburst floods (GLOFs)[5,93], while substantially reducing long-term meltwater availability during dry seasons[94,95]. In contrast, low-emission scenarios (SSP126) project a much lower and more constrained glacier mass loss rate of -2.3 ± 0.3 Gt/yr, reflecting both reduced sensitivity to warming and substantially lower uncertainty, thereby preserving a larger fraction of cryospheric water storage[96]. These contrasting uncertainty ranges underscore the critical role of emission mitigation in limiting both the magnitude and unpredictability of future glacier mass loss. From a policy perspective, adaptive strategies should prioritize enhanced glacier and hydrological monitoring, climate-resilient water allocation, early-warning systems for glacier-related hazards, and the integration of cryospheric change into regional water and agricultural planning[2,6,97,98]. Such measures are essential to reduce vulnerability and support long-term adaptation in glacier-dependent regions under a changing climate.

Materials and methods

HMA is one of the world's most climatically diverse and topographically complex regions, spanning approximately 5 million square kilometers across countries such as China, India, Nepal, Bhutan, Pakistan, Afghanistan, and several Central Asian nations[99,100]. It includes major mountain ranges like the Himalayan, Karakoram, Hindu Kush, Pamir, and Tien Shan Mountain ranges[101,102]. The region lies between 25°N to 45°N latitude and 65°E to 105°E longitude, with an average elevation of 4000 m above sea level (asl) elevations ranging from foothills to peaks exceeding 8,000 m, such as Mount Everest (8,848 m) and K2 (8,611 m)[101]. HMA hosts over 95,534 glaciers covering an area of approximately 100,000 square kilometers[103,104], feeding major river systems like the Indus, Ganges, Brahmaputra, Mekong, Yellow, Salween and Yangtze, which sustain billions of people downstream[101]. The region is home to numerous hydropower projects, with major installations along rivers like the Indus (e.g., Tarbela Dam in Pakistan), the Ganges (e.g., Tehri Dam in India), and the Yangtze (e.g., Three Gorges Dam in China). These projects are pivotal for regional energy security[105,106].

HMA encompasses a diverse array of climate zones, ranging from arid and semi-arid conditions in the western and central regions to humid subtropical climates in the eastern Himalayas[1]. These zones are shaped by the interplay of the South Asian Summer Monsoon and mid-latitude westerlies. The eastern Himalayas experienced heavy monsoonal rainfall, leading to dense vegetation and relatively high humidity[107]. In contrast, the western regions, including the Karakoram and Hindu Kush, are predominantly influenced by westerly disturbances, resulting in colder and drier conditions with significant snow accumulation in winter[108]. The Tibetan Plateau, mainly characterized by an alpine tundra climate with extreme temperature variations and low precipitation, primarily in the form of snow[109]. These distinct climate zones influence the distribution of glaciers, vegetation, and water resources, underpinning the region's ecological and hydrological significance. Figure 5 illustrates the topography of the HMA and its 15 sub-regions, along with glacier boundaries from the Randolph Glacier Inventory[110]. The total glacier area, derived from RGI7, is 99,468 km^2, with the largest share in Karakoram (21.5%) and the smallest in Qilian Shan (1.7%). The distribution of glacier area, grid area, number of

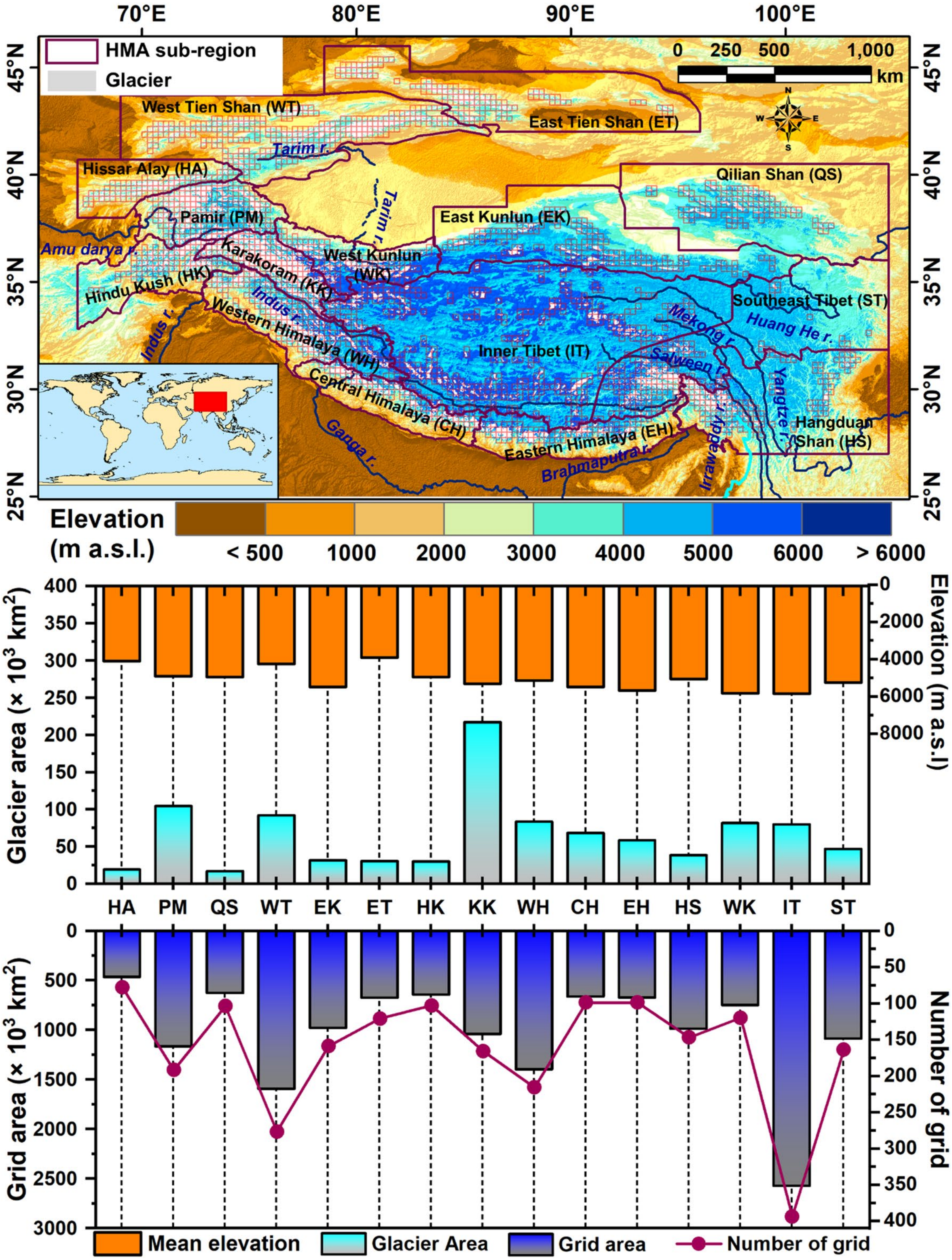

Fig. 5. Distribution of topography in High Mountain Asia (HMA) and its sub-regions, showing major rivers, glacier boundaries, and grids. The graph displays the distribution of glacier area, grid area, number of grids, and mean elevation of glaciers in the 15 sub-regions of HMA.

grids, and mean elevation of glaciers in the 15 sub-regions of HMA is also depicted. The grid-wise glacier area percentage is shown in Fig. S4.

In this study, GRACE and GRACE-FO TWSA mascon solutions are employed for glacier mass change analysis. The GRACE dataset spans from April 2002 to May 2017, while GRACE-FO data are available from July 2018 onward. Three agencies provide mascon solutions with different processing approaches. We use the Center for Space Research (CSR) TWSA RL06.2 data from the University of Texas at Austin[111], available at high spatial resolution (0.25° equatorial grid, ~ 25 km). Additionally, these data include ocean and land masks to minimize leakage errors along coastlines. Jet Propulsion Laboratory (JPL) TWSA RL06.3Mv04 data are retrieved from the Physical Oceanography Distributed Active Archive Center (PODAAC)[112], available at 0.5° equatorial grid (~ 56 km). German Research Center for Geosciences (GFZ) TWSA RL06v2.0 data at 0.5° grid resolution from the Goddard Space Flight Center (GSFC)[113] are also used. These mascons represent anomalies relative to the baseline period of January 2000 to December 2009. GRACE and GRACE-FO datasets contain gaps due to technical issues with approximately 20 months of missing data in GRACE, two months in GRACE-FO, and an 11-month gap between the two missions (Fig. S5). To reduce uncertainties arising from processing differences, we average the three mascon solutions (Fig. S6), as recommended by[84].

The change in TWSA over a glaciated grid cell can be defined by Eq. 1.

$$TWSA_{GRACE} = (SM + SWE + CW + GMC)_{anomalies} \tag{1}$$

where SM, SWE, CW, and GMC represent soil moisture, snow water equivalent, canopy water, and glacier mass change, respectively.

The GLDAS Noah Land Surface Model L4[86] dataset is utilized. GLDAS terrestrial water storage (TWS) is calculated as the sum of SM storage across four layers (0–2 m depth), CW storage, and SWE. Therefore, the GLDAS TWS is defined by Eq. 2.

$$TWS_{model} = CW + SM + SWE \tag{2}$$

The TWS_{model} is converted into an anomaly using the mean mass change from January 2004 to December 2009, consistent with the GRACE TWSA, as done in previous studies[22,34,87,114], and is defined by Eq. 3.

$$TWSA_{model} = TWS_{model} - \mu\ (TWS_{model})_{2004-2009} \tag{3}$$

The GMC can be derived using Eqs. 1 and 3, defined by Eq. 4.

$$GMC = TWSA_{GRACE} - TWSA_{model} \tag{4}$$

The $TWSA_{model}$ represents the model-derived anomaly, calculated in the same way as the GRACE TWSA. The GMC represents the combined effect of mass change in each grid cell due to glacier or glacier lake changes.

For climatic and radiative fluxes, we used ERA5-Land[115] for air temperature (T_a), incoming shortwave (SWI), and longwave radiation (LWI), and specific humidity (SH), derived from relative humidity and surface pressure, on a spatial resolution (~ 9 km) with monthly timescale. ERA5-Land has been shown to outperform other reanalysis datasets in mountainous regions, providing more accurate daily precipitation estimates[116]. However, it does not assimilate observations from meteorological stations, leading to potential discrepancies in areas with snow cover and soil moisture variability[117]. Some studies also report precipitation overestimation in certain regions[118]. Despite these limitations, continuous improvements in modeling techniques and data assimilation enhance their reliability for environmental applications[119].

Therefore, the precipitation data are retrieved from the Integrated Multi-satellite Retrievals for Global Precipitation Measurement (IMERG) Version 07 Level 3 "Final Run" daily product, which provides a spatial resolution of 0.1° × 0.1°. This version offers improved accuracy and consistency by incorporating the most comprehensive input data and post-processing algorithms. Previous studies have demonstrated that IMERG outperforms many other precipitation datasets in terms of accuracy and reliability[116].

For land surface temperature (T_s) variation across glacier grids in the HMA, we used mean monthly products from moderate resolution imaging spectroradiometer (MODIS) Terra (MOD11C3) and Aqua (MYD11C3), available both day and night on a global scale. We derived mean monthly values by averaging the four images per month at 0.05° resolution for the period April 2002 to December 2023.

For future scenarios data, we use the ISIMIP3b dataset to analyze future glacier mass changes. Each SSP scenario contains five bias-corrected GCMs at a global scale: MPI-ESM1-2-HR, UKESM1-0-LL, GFDL-ESM4, IPSL-CM6A-LR, and MRI-ESM2- 0. Table S2 lists general information on these representative GCMs, originally published in CMIP6. We utilize five variables: P, SH, T_a, SWI, and LWI. The dataset is available at daily and 0.5° grid resolution. Our assessment shows that the simulations from the five GCMs align well with ERA5-Land observations, particularly for temperature and radiation (Fig. S7). Similarly, GCMs based precipitation well correlated with IMERG precipitation (Fig. S7), we use the ensemble mean of the five models to reduce uncertainty, as demonstrated by previous studies[49,120].

ISIMIP3b provides widely used bias-corrected GCM data globally but evaluating their performance for our study area is essential. We estimate the ensemble mean of the five GCMs for the historical period (1981–2014) and the future period (2015–2100) under low (SSP126) and high (SSP585) emission scenarios. Historical data and reference data (ERA5-Land) from 1981 to 2014 (except P, 1998–2014) are used for bias correction using methods from[121,122]. Bias correction of daily P, T_a, SH, SWI and LWI was performed using monthly correction factors derived from historical GCMs output and ERA5-Land data for the period 1981–2014. The spatial mean monthly bias correction factors for each variables are given in Table S3.

The missing values of 33 months in the GRACE datasets were filled using eight input variables as predictors explained in[32] based on MissForest algorithm[31]. The MissForest model is trained using detrended hydroclimatic variables and the target variable ($\mathrm{TWSA_{GRACE}}$) to predict the missing values. The datasets are detrended using the STL[123]. By leveraging the predictive power of RF model[124], MissForest preserves the relationships between variables and provides accurate imputations, making it an effective choice for filling missing values in hydrological data[125–127]. The maximum number of iterations was set to 10, with 100 trees used to train the MissForest model.

We employed a GAM to predict GMC using five climate predictors: P, $\mathrm{T_a}$, SH, SWI, and LWI. GAM extends generalized linear models by fitting smooth, nonlinear functions to capture complex relationships between predictors and the target[128,129]. The historical data (2002–2023) were split into 70% training and 30% testing sets to train and evaluate model performance. The trained model was then applied to CMIP6 projections for 2024–2099, evaluating early- (2024–2049), mid- (2050–2075), and late-future (2076–2100) periods. GAM's flexibility and smoothing constraints allow it to effectively model nonlinear climate impacts on GMC, while avoiding overfitting. The degree of smoothness for each predictor was set using the smoothing parameter k, which determines the maximum number of basis functions for the smooth term. The actual smoothness was optimized automatically through generalized cross-validation to balance flexibility and predictive accuracy. This ensures that the fitted functions are neither too rigid nor overly complex, providing robust and interpretable relationships between climate variables and GMC. Due to this combination of flexibility and interpretability, GAMs are widely used for predicting future climate-driven changes[25,50,51].

Model performance was evaluated using R^2 and RMSE, which are widely used metrics for assessing machine learning and deep learning model performance[130–132]. For training and testing the machine learning model, all variables are standardized to a mean of zero and a standard deviation of one to improve the model's efficiency, stability, and accuracy, especially when handling diverse datasets. Standardization ensures that variables are on a comparable scale, which is crucial for effective model training. The spatial trend and its statistical significance are assessed using Sen's slope estimator[133] and the Mann-Kendall (MK) trend test[134] at a 95% confidence interval. Sen's slope measures the magnitude of a trend, while the MK test evaluates whether the trend is statistically significant. The overall workflow of the methodology is shown in Fig. 6.

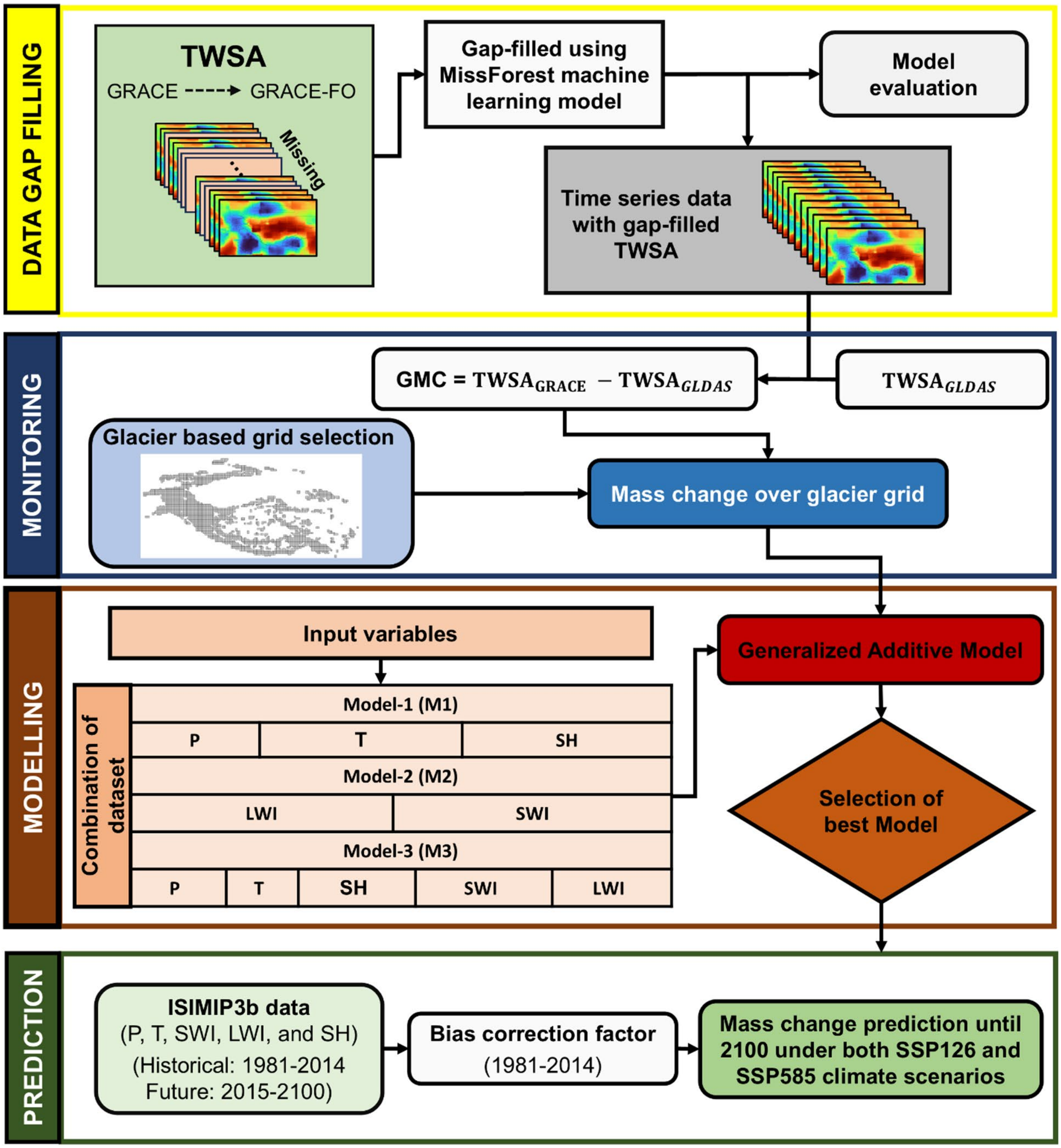

Fig. 6. Overall workflow of the methodology used in this study.

Data availability

The datasets and code generated and/or analyzed in this study are available on request. Other datasets were downloaded from various sources such as GRACE CSR mascon [111], JPL mascon [112], GSFC mascon [113], ERA5 Land [135], Randolph Glacier Inventory[110], GLDAS Noah Land Surface Model [136], Integrated Multi-satellite Retrievals for Global Precipitation Measurement (IMERG) [137], MODIS Land Surface Temperature [138], and ISIMIP [139].

Received: 19 September 2025; Accepted: 4 February 2026
Published online: 13 February 2026

References

1. Bhattacharya, A. et al. High mountain Asian glacier response to climate revealed by multi-temporal satellite observations since the 1960s. *Nat. Commun.* **12**, 1–13 (2021).

2. Immerzeel, W. W., Van Beek, L. P. H. & Bierkens, M. F. P. Climate change will affect the Asian water towers. *Sci. (1979)*. **328**, 1382–1385 (2010).
3. Immerzeel, W. W. et al. Importance and vulnerability of the world's water towers. *Nature* **577**, 364–369 (2020).
4. Nie, Y. et al. Glacial change and hydrological implications in the himalaya and Karakoram. *Nat. Rev. Earth Environ.* **2**, 91–106 (2021).
5. Bolch, T. et al. The state and fate of Himalayan glaciers. *Sci. (1979)*. **336**, 310–314 (2012).
6. Biemans, H. et al. Importance of snow and glacier meltwater for agriculture on the Indo-Gangetic plain. *Nat. Sustain.* **2**, 594–601 (2019).
7. Gafurov, A. et al. GRACE observes the natural and irrigation-induced regional redistribution of water storage in central Asia. *J Hydrol. Reg. Stud* **56**, (2024).
8. Wang, Q., Yi, S. & Sun, W. Continuous Estimates of Glacier Mass Balance in High Mountain Asia Based on ICESat-1,2 and GRACE/GRACE Follow-On Data. *Geophysical Research Letters* vol. 48 Preprint at (2021). https://doi.org/10.1029/2020GL090954
9. Mo, Y. S., Li, X. D. & Xu, M. Regional differences in glacier changes and responses to climate warming in Asia. *Res. Cold Arid Reg.* https://doi.org/10.1016/j.rcar.2024.12.004 (2024).
10. Yao, T. et al. Different glacier status with atmospheric circulations in Tibetan plateau and surroundings. *Nat. Clim. Chang.* **2**, 663–667 (2012).
11. Kääb, A., Berthier, E., Nuth, C., Gardelle, J. & Arnaud, Y. Contrasting patterns of early twenty-first-century glacier mass change in the Himalayas. *Nature* **488**, 495–498 (2012).
12. Angchuk, T. et al. Annual and seasonal glaciological mass balance of Patsio Glacier, Western himalaya (India) from 2010 to 2017. *J. Glaciol.* 1–10. https://doi.org/10.1017/jog.2021.60 (2021).
13. Soheb, M. et al. Wintertime surface energy balance of a high-altitude seasonal snow surface in Chhota Shigri glacier basin, Western himalaya. *Geol. Soc. Spec. Publ.* **462**, 155–168 (2018).
14. Bandyopadhyay, D., Singh, G. & Kulkarni, A. V. Glacier ice mass changes in central Himalayas during 2000–2014 using TanDEM-X data. *Int. Archives Photogrammetry Remote Sens. Spat. Inform. Sci. - ISPRS Archives*. **42**, 193–196 (2018).
15. Bandyopadhyay, D., Singh, G. & Kulkarni, A. V. Glacier elevation and mass changes in Himalayas during 2000–2014. *The Cryosphere Discussions [preprint]* 1–16 (2019). https://doi.org/10.5194/tc-2019-85
16. Patel, A. et al. Monitoring glacier characteristics and their mass balance using a multidimensional approach over the glaciers of the Chandra basin, Western himalaya. *Hydrol. Sci. J.* **67**, 419–435 (2022).
17. Patel, A. et al. Estimation of mass and energy balance of glaciers using a distributed energy balance model over the Chandra river basin (Western Himalaya). *Hydrol. Process.* **35**, 1–22 (2021).
18. Tawde, S. A., Kulkarni, A. V. & Bala, G. An estimate of glacier mass balance for the Chandra basin, Western Himalaya, for the period 1984–2012. *Ann. Glaciol*. **58**, 99–109 (2017).
19. Sahu, R., Gupta, R. D., Ramanathan, A., Kumar, P. & Eidhammer, T. Long-term annual and seasonal mass balance reconstruction and sensitivity analysis of Chhota Shigri glacier in Western himalaya. *Environ. Sci. Pollut. Res.* **31**, 4910–4924 (2024).
20. Landerer, F. W. et al. Extending the global mass change data record: GRACE Follow-On instrument and science data performance. *Geophys. Res. Lett.* **47**, 1–10 (2020).
21. Tapley, B. D. et al. Contributions of GRACE to Understanding climate change. *Nat. Clim. Chang.* **9**, 358–369 (2019).
22. Zhou, S. et al. Has the Karakoram anomaly persisted over the past two decades? *GIsci Remote Sens.* **62**, (2025).
23. Rodell, M. et al. Emerging trends in global freshwater availability. *Nature* **557**, 651–659 (2018).
24. Humphrey, V., Gudmundsson, L. & GRACE-REC: A reconstruction of climate-driven water storage changes over the last century. *Earth Syst. Sci. Data.* **11**, 1153–1170 (2019).
25. Arshad, A. et al. Multi-model ensemble machine learning-based downscaling and projection of GRACE data reveals groundwater decline in Saudi Arabia throughout the 21st century. *J. Hydrol. Reg. Stud.* **60**, 102552 (2025).
26. Li, F. et al. Comparison of Data-Driven techniques to reconstruct (1992–2002) and predict (2017–2018) GRACE-Like gridded total water storage changes using climate inputs. *Water Resour. Res.* **56**, 1–36 (2020).
27. Dharpure, J. K., Howat, I. M., Kaushik, S. & Mark, B. G. Combining machine learning algorithms for bridging gaps in GRACE and GRACE Follow-On missions using ERA5-Land reanalysis. *Sci. Remote Sens.* **11**, 100198 (2025).
28. Uz, M. et al. Bridging the gap between GRACE and GRACE-FO missions with deep learning aided water storage simulations. *Science Total Environment* **830**, (2022).
29. Sun, Z., Long, D., Yang, W., Li, X. & Pan, Y. Reconstruction of GRACE data on changes in total water storage over the global land surface and 60 basins. *Water Resource Res.* **1–21** https://doi.org/10.1029/2019WR026250 (2020).
30. Mo, S. et al. Bayesian convolutional neural networks for predicting the terrestrial water storage anomalies during GRACE and GRACE-FO gap. *J Hydrol. (Amst)* **604**, (2022).
31. Stekhoven, D. J. & Bühlmann, P. Missforest-Non-parametric missing value imputation for mixed-type data. *Bioinformatics* **28**, 112–118 (2012).
32. Dharpure, J. K., Howat, I. M. & Kaushik, S. Declining groundwater storage in the indus basin revealed using GRACE and GRACE-FO data. *Water Resource Res.* **61**, e2024WR038279 (2025).
33. Ciracì, E., Velicogna, I. & Swenson, S. Continuity of the mass loss of the world's glaciers and ice caps from the GRACE and GRACE Follow-On missions. *Geophys. Res. Lett.* **47**, 1–11 (2020).
34. Patel, A. et al. Regional mass variations and its sensitivity to climate drivers over glaciers of Karakoram and Himalayas. *GIsci Remote Sens.* **00**, 1–23 (2021).
35. Brun, F., Berthier, E., Wagnon, P., Kääb, A. & Treichler, D. A spatially resolved estimate of high mountain Asia glacier mass balances from 2000 to 2016. *Nat. Geosci.* **10**, 668–673 (2017).
36. Sakai, A. & Fujita, K. Contrasting glacier responses to recent climate change in high- mountain Asia. *Sci. Rep.* 1–8. https://doi.org/10.1038/s41598-017-14256-5 (2017).
37. Xiang, L. et al. Glacier mass balance in high mountain Asia inferred from a GRACE release-6 gravity solution for the period 2002–2016. *J. Arid Land.* **13**, 224–238 (2021).
38. Bolibar, J. et al. Deep learning applied to glacier evolution modelling. *Cryosphere* **14**, 565–584 (2020).
39. Bolibar, J., Rabatel, A., Gouttevin, I., Zekollari, H. & Galiez, C. Nonlinear sensitivity of glacier mass balance to future climate change unveiled by deep learning. *Nat. Commun.* **13**, 1–11 (2022).
40. Wiltshire, A. J. Climate change implications for the glaciers of the Hindu Kush, Karakoram and Himalayan region. *Cryosphere* **8**, 941–958 (2014).
41. Zhao, H., Su, B., Lei, H., Zhang, T. & Xiao, C. A new projection for glacier mass and runoff changes over high mountain Asia. *Sci. Bull. (Beijing)*. **68**, 43–47 (2023).
42. Zhao, L., Ding, R. & Moore, J. C. Glacier volume and area change by 2050 in high mountain Asia. *Glob Planet. Change*. **122**, 197–207 (2014).
43. Lange, S. Trend-preserving bias adjustment and statistical downscaling with ISIMIP3BASD (v1.0). *Geosci. Model. Dev.* **12**, 3055–3070 (2019).
44. Hempel, S., Frieler, K., Warszawski, L., Schewe, J. & Piontek, F. A trend-preserving bias correction – The ISI-MIP approach. *Earth Sys. Dyn.* **4**, 219–236 (2013).
45. Zekollari, H. et al. Glacier preservation doubled by limiting warming to 1.5°C versus 2.7°C. *Sci. (1979)*. **388**, 979–983 (2025).

46. Huo, F., Li, Z., Li, Y., Famiglietti, J. S. & Chandanpurkar, H. A. Can climate change signals be detected from the terrestrial water storage at daily timescale ? *Clim. Atmospheric Sci.* 1–12. https://doi.org/10.1038/s41612-024-00646-w (2024).
47. Pokhrel, Y. et al. Global terrestrial water storage and drought severity under climate change. *Nat. Clim. Chang.* **11**, 226–233 (2021).
48. Xu, F. et al. Understanding climate change impacts on drought in China over the 21st century: a multi-model assessment from CMIP6. *NPJ Clim. Atmos. Sci* **7**, (2024).
49. He, S., Chen, K., Liu, Z. & Deng, L. Exploring the impacts of climate change and human activities on future runoff variations at the seasonal scale. *J. Hydrol. (Amst).* **619**, 129382 (2023).
50. Murphy, R. R., Perry, E., Harcum, J. & Keisman, J. A generalized additive model approach to evaluating water quality: Chesapeake Bay case study. *Environ. Model Softw.* **118**, 1–13 (2019).
51. Wood, S. N. Inference and computation with generalized additive models and their extensions. *Test* **29**, 307–339 (2020).
52. Arshad, A., Mirchi, A., Taghvaeian, S. & Aghakouchak, A. Downscaled - GRACE data reveal anthropogenic and Climate - Induced water storage decline across the indus basin. *Water Resource Res.* **60**, e2023WR035882 (2024).
53. Ali, S. et al. The GWR model-based regional downscaling of GRACE/GRACE-FO derived groundwater storage to investigate local-scale variations in the North China plain. *Sci. Total Environ.* **908**, 168239 (2024).
54. Harpold, A. A. & Brooks, P. D. Humidity determines snowpack ablation under a warming climate. *Proc. Natl. Acad. Sci. U S A.* **115**, 1215–1220 (2018).
55. Aubry-Wake, C., Zéphir, D., Baraer, M., McKenzie, J. M. & Mark, B. G. Importance of longwave emissions from adjacent terrain on patterns of tropical glacier melt and recession. *J. Glaciol.* **64**, 49–60 (2018).
56. Shean, D. E. et al. A Systematic, regional assessment of high mountain Asia glacier mass balance. *Front. Earth Sci. (Lausanne).* **7**, 1–19 (2020).
57. Wouters, B., Gardner, A. S. & Moholdt, G. Global glacier mass loss during the GRACE satellite mission (2002–2016). *Front. Earth Sci. (Lausanne).* **7**, 1–11 (2019).
58. Guan, W. et al. Updated Surge-Type glacier inventory in the West Kunlun Mountains, Tibetan Plateau, and implications for glacier change. *J. Geophys. Res. Earth Surf.* **127**, 1–17 (2022).
59. Zhang, Z. et al. Glacier mass changes over Duxueshan, Burog Kangri, and Zangser Kangri in the inner Tibetan plateau. *Environ. Earth Sci.* **79**, 1–13 (2020).
60. Gardner, A. S. et al. A reconciled estimate of glacier contributions to sea level rise: 2003 to 2009. *Science (1979).* 340, 852–857 (2013).
61. Yi, S. & Sun, W. Evaluation of glacier changes in high-mountain Asia based on 10 year GRACE RL05 models. *J. Geophys. Res. Solid Earth.* **119**, 2504–2517 (2014).
62. Maurer, J. M., Schaefer, J. M., Rupper, S. & Corley, A. Acceleration of ice loss across the Himalayas over the past 40 years. *Sci Adv* **5**, (2019).
63. Zhang, Y. & Kang, S. Melting glaciers threaten ice core science on the Tibetan plateau. *Nat. Geosci.* **16**, 656–657 (2023).
64. Kumar, P. et al. Response of Karakoram-Himalayan glaciers to climate variability and Climatic change: A regional climate model assessment. *Geophys. Res. Lett.* **42**, 1818–1825 (2015).
65. Zhang, G., Yao, T., Xie, H., Kang, S. & Lei, Y. Increased mass over the Tibetan plateau: from lakes or glaciers? *Geophys. Res. Lett.* **40**, 2125–2130 (2013).
66. De Kok, R. J., Tuinenburg, O. A., Bonekamp, P. N. J. & Immerzeel, W. W. Irrigation as a potential driver for anomalous glacier behavior in high mountain Asia. *Geophys. Res. Lett.* **45**, 2047–2054 (2018).
67. Moch, J. M. et al. Aerosol-Radiation interactions in China in winter: competing effects of reduced shortwave radiation and Cloud-Snowfall-Albedo feedbacks under rapidly changing emissions. *J. Geophys. Research: Atmos.* **127**, 1–20 (2022).
68. Rangwala, I., Miller, J. R. & Xu, M. Warming in the Tibetan plateau: possible influences of the changes in surface water vapor. *Geophys. Res. Lett.* **36**, 1–6 (2009).
69. Yang, K. et al. Recent climate changes over the Tibetan plateau and their impacts on energy and water cycle: A review. *Glob Planet. Change.* **112**, 79–91 (2014).
70. Carrivick, J. L. et al. Accelerating glacier area loss across the Andes since the little ice age. *Geophys Res. Lett* **51**, (2024).
71. Linsbauer, A., Huss, M., Hodel, E., Bauder, A. & Barandun, M. Vanished glaciers of the Swiss alps: an inventory-based assessment from 1973 to 2016. *Ann. Glaciol.* https://doi.org/10.1017/aog.2025.10031 (2025).
72. Mernild, S. H. et al. Mass loss and imbalance of glaciers along the Andes cordillera to the sub-Antarctic Islands. *Glob Planet. Change.* **133**, 109–119 (2015).
73. Zheng, W. et al. Community estimate of global glacier mass changes from 2000 to 2023. *Nature* **639**, 382–388 (2025).
74. Zemp, M. et al. Global glacier mass changes and their contributions to sea-level rise from 1961 to 2016. *Nature* **568**, 382–386 (2019).
75. Jakob, L. & Gourmelen, N. Glacier mass loss between 2010 and 2020 dominated by atmospheric forcing. *Geophys Res. Lett* **50**, (2023).
76. Thibert, E., Dkengne Sielenou, P., Vionnet, V., Eckert, N. & Vincent, C. Causes of glacier melt extremes in the alps since 1949. *Geophys. Res. Lett.* **45**, 817–825 (2018).
77. Gobiet, A. et al. 21st century climate change in the European Alps—a review. *Sci. Total Environ.* **493**, 1138–1151 (2014).
78. Davaze, L., Rabatel, A., Dufour, A., Hugonnet, R. & Arnaud, Y. Region-Wide annual glacier surface mass balance for the European alps from 2000 to 2016. *Front. Earth Sci. (Lausanne).* **8**, 0–14 (2020).
79. Weifeng, X. et al. Multi-source DEM accuracy evaluation based on ICESat-2 in Qinghai-Tibet Plateau, China. *Int. J. Digit. Earth.* **17**, 1–24 (2024).
80. Fan, Y. et al. Glacier mass-balance estimates over high mountain Asia from 2000 to 2021 based on ICESat-2 and NASADEM. *J. Glaciol.* **1–13** https://doi.org/10.1017/jog.2022.78 (2022).
81. Taubenberger, C. J., Felikson, D. & Neumann, T. Brief communication: preliminary ICESat-2 (Ice, cloud and land elevation Satellite-2) measurements of outlet glaciers reveal heterogeneous patterns of seasonal dynamic thickness change. *Cryosphere* **2**, 1341–1348 (2022).
82. Wagnon, P. et al. Reanalysing the 2007-19 glaciological mass-balance series of Mera Glacier, Nepal, central Himalaya, using geodetic mass balance. *J. Glaciol.* **67**, 117–125 (2021).
83. Kumar, A. et al. Estimation of recent changes in thickness and mass balance of the Patsio glacier in the great Himalayan region using geodetic technique and ancillary data. *Geocarto Int.* **0**, 1–17 (2018).
84. Landerer, F. W. & Cooley, S. W. *GRACE D-103133 Gravity Recovery and Climate Experiment Level-3 Data Product User Handbook*. (2021).
85. Sakumura, C., Bettadpur, S. & Bruinsma, S. Ensemble prediction and intercomparison analysis of GRACE time-variable gravity field models. *Geophys. Res. Lett.* **41**, 1389–1397 (2014).
86. Rodell, M. et al. The global land data assimilation system. *American Meteorological Society* (2004).
87. Jiao, J. et al. Interannual glacier and lake mass changes over Scandinavia from GRACE. *Geophys. J. Int.* **221**, 2126–2141 (2020).
88. Muñoz-Sabater, J. et al. ERA5-Land: A state-of-the-art global reanalysis dataset for land applications. *Earth Syst. Sci. Data.* **13**, 4349–4383 (2021).
89. Rui, H., Beaudoing, H. & Loeser, C. README document for GLDAS version 2 data products. *Goddard Earth Sci. Data Inform. Serv. Cent. (GES DISC).* **16**, 1–32 (2015).

90. Bikse, J., Retike, I., Haaf, E. & Kalvans, A. Assessing automated gap imputation of regional scale groundwater level data sets with typical gap patterns. *J. Hydrol. (Amst).* 620, 129424 Contents (2023).
91. Sutterley, T. C., Velicogna, I. & Hsu, C. W. Self-Consistent ice mass balance and regional sea level from Time-Variable gravity. *Earth Space Science* **7**, (2020).
92. Baumann, S. Comparison of glacier mass balance data in the Tien Shan and Pamir, central Asia. *Arct. Antarct. Alp. Res.* **49**, 133–146 (2017).
93. Dubey, S. & Goyal, M. K. Glacial lake outburst flood Hazard, downstream Impact, and risk over the Indian Himalayas. *Water Resour. Res.* **56**, 1–21 (2020).
94. Pritchard, H. D. Asia's shrinking glaciers protect large populations from drought stress. *Nature* **569**, 649–654 (2019).
95. Kaser, G., Großhauser, M. & Marzeion, B. Contribution potential of glaciers to water availability in different climate regimes. (2010). (2010).
96. Rounce, D. R. et al. Global glacier change in the 21st century: every increase in temperature matters. *Sci. (1979).* **379**, 78–83 (2023).
97. Halea, S. & Hydrology Current research implications of climate change on Glacier-melt hydrology in high mountain regions. *Hydrology: Curr. Res.* **14**, 3–4 (2023).
98. Huss, M. & Hock, R. Global-scale hydrological response to future glacier mass loss. *Nat. Clim. Chang.* **8**, 135–140 (2018).
99. Khanal, S., Tiwari, S., Lutz, A. F., Hurk, B. V. D. & Immerzeel, W. W. Historical climate trends over high mountain Asia derived from ERA5 reanalysis data. *J. Appl. Meteorol. Climatol.* **62**, 263–288 (2023).
100. Yao, T. et al. Third pole environment (TPE). *Environ. Dev.* **3**, 52–64 (2012).
101. Lalande, M., Ménégoz, M., Krinner, G., Naegeli, K. & Wunderle, S. Climate change in the high mountain Asia in CMIP6. *Earth Sys. Dyn.* **12**, 1061–1098 (2021).
102. Guo, L. et al. A new inventory of high mountain Asia surging glaciers derived from multiple elevation datasets since the 1970s. *Earth Syst. Sci. Data.* **15**, 2841–2861 (2023).
103. Farinotti, D. et al. A consensus estimate for the ice thickness distribution of all glaciers on Earth. *Nat. Geosci.* **12**, 168–173 (2019).
104. Yang, L. et al. Historical and projected evolutions of glaciers in response to climate change in high mountain Asia. *Environ. Res.* **237**, 117037 (2023).
105. Sundaram, S., Sharma, S., Mathur, R., Kashyap, K. & Verma, K. A case study of the Background, Aspects, and impacts of the Tehri dam on the Economy, ecology & population of India. *International J. Innov. Multidisciplinary Research* **3**, (2023).
106. Salazar, J. G. Damming the child of the ocean: the three Gorges project. *J. Environ. Dev.* **9**, 160–174 (2000).
107. Kad, P. & Ha, K. J. Recent tangible natural variability of monsoonal orographic rainfall in the Eastern Himalayas. *Journal Geophys. Research: Atmospheres* **128**, (2023).
108. Cannon, F., Carvalho, L. M. V., Jones, C. & Bookhagen, B. Multi-annual variations in winter Westerly disturbance activity affecting the himalaya. *Clim. Dyn.* **44**, 441–455 (2014).
109. Latif, A. et al. Review on global change status and its impacts on the Tibetan plateau environment. *J. Plant. Ecol.* **12**, 917–930 (2019).
110. RGI 7.0. Randolph Glacier Inventory - A Dataset of Global Glacier Outlines, Version 7.0. *NSIDC: National Snow and Ice Data Center, Boulder, Colorado USA* (2023). https://doi.org/https://www.glims.org/RGI/ doi:https://www.glims.org/RGI/
111. Save, H. CSR GRACE and GRACE-FO RL06 Mascon Solutions v02 [Dataset]. (2020).
112. Wiese, D. N. JPL GRACE Mascon Ocean, Ice, and Hydrology Equivalent Water Height CRI Filtered [Dataset]. (2018).
113. Loomis, B. D. High-spatial-resolution mass rates from GRACE and GRACE-FO: global and ice sheet analyses [Dataset]. *J Geophys. Res. Solid Earth* (2021).
114. Hussain, D. et al. Spatial and Temporal variations of terrestrial water storage in upper indus basin using GRACE and altimetry data. *IEEE Access.* **8**, 65327–65339 (2020).
115. Muñoz Sabater, J. ERA5-Land hourly data from 1950 to present. *Copernicus Clim. Change Service (C3S) Clim. Data Store*. https://doi.org/10.24381/cds.e2161bac (2019).
116. Xin, Y. et al. Evaluation of IMERG and ERA5 precipitation products over the Mongolian plateau. *Sci. Rep.* **12**, 1–26 (2022).
117. Clelland, A. A., Marshall, G. J. & Baxter, R. Evaluating the performance of key ERA-Interim, ERA5 and ERA5-Land climate variables across Siberia. *Int. J. Climatol.* **44**, 2318–2342 (2024).
118. Zhang, Y. et al. Error decomposition of CRA40-Land and ERA5-Land reanalysis precipitation products over the Yongding river basin in North China. *Atmosphere (Basel)* 13, (2022).
119. Eicker, A. et al. Daily GRACE satellite data evaluate short-term hydro-meteorological fluxes from global atmospheric reanalyses. *Sci. Rep.* **10**, 1–10 (2020).
120. de Coelho, G. A. et al. Potential impacts of future extreme precipitation changes on flood engineering design across the contiguous united States. *Water Resour. Res* **58**, (2022).
121. Srivastava, S. & Azam, M. F. Mass- and Energy-Balance modeling and sublimation losses on Dokriani Bamak and Chhota Shigri glaciers in himalaya since 1979. *Front. Water*. **4**, 1–21 (2022).
122. Sharma, A. & Kumar, M. Assessment of the changes in precipitation and temperature in Teesta river basin in Indian Himalayan region under climate change. *Atmos. Res.* **231**, 104670 (2020).
123. Cleveland, R. B., Cleveland, W. S., McRea, J. E. & Terpenning, I. STL: A Seasonal-Trend decomposition procedure based on loess. *J. Off Stat.* **6**, 3–73 (1990).
124. Breiman, L. Random forests. *Mach. Learn.* **45**, 5–32 (2001).
125. Addi, M., Gyasi-agyei, Y., Obuobie, E. & Kofitse, L. Evaluation of imputation techniques for infilling missing daily rainfall records on river basins in Ghana. *Hydrol. Sci. J.* **00**, 1–15 (2022).
126. Zhou, Y., Tang, Q. & Zhao, G. Gap infilling of daily streamflow data using a machine learning algorithm (MissForest) for impact assessment of human activities. *J. Hydrol. (Amst).* **627**, 130404 (2023).
127. Arriagada, P., Karelovic, B. & Link, O. Automatic gap-filling of daily streamflow time series in data-scarce regions using a machine learning algorithm. *J. Hydrol. (Amst).* **598**, 126454 (2021).
128. Wood, S. & Mixed, G. A. M. Computation Vehicle with GCV/AIC/REML/NCV smoothness estimation and GAMMs by REML/PQL. (2018).
129. Jones, K. & Almond, S. Moving out of the linear rut: the possibilities of generalized additive models. *Transactions Inst. Br. Geographers* 434–447 (1992).
130. Adnan, R. M. et al. Application of soft computing models in streamflow forecasting. *Proc. Inst. Civil Eng. Water Manag.* **172**, 123–134 (2019).
131. Hussain, D., Hussain, T., Khan, A. A., Naqvi, S. A. A. & Jamil, A. A deep learning approach for hydrological time-series prediction: A case study of Gilgit river basin. *Earth Sci. Inf.* **13**, 915–927 (2020).
132. Alizadeh, M. J., Rajaee, T. & Motahari, M. Flow forecasting models using hydrologic and hydrometric data. *Proceedings of the Institution of Civil Engineers: Water Management* 170, 150–162 (2017).
133. Sen, P. K. Estimates of the regression coefficient based on kendall's Tau. *J. Am. Stat. Assoc.* **63**, 1379–1389 (1968).
134. Mann, H. B. Nonparametric tests against trend. *Econometrica* **13**, 245–259 (1945).
135. Muñoz Sabater, J. ERA5-Land monthly averaged data from 1950 to present [Dataset]. *Copernicus Climate Change Service (C3S)* (2022).
136. Rodell, M. et al. The global land data assimilation system. *Bull. Am. Meteorol. Soc.* **85**, 381–394 (2004).

137. NASA Earthdata. Integrated Multi-satellite Retrievals for Global Precipitation Measurement (IMERG) Version 07 Level 3 [Data set]. (2025). https://search.earthdata.nasa.gov/?q=GLDAS%20Noah%20Land%20Surface
138. NASA Earthdata. MODIS/Terra Land Surface Temperature/Emissivity Monthly L3 Global 0.05Deg CMG V061. (2025). https://search.earthdata.nasa.gov/
139. ISIMIP. The Inter-Sectoral Impact Model Intercomparison Project [Data set]. (2025). https://www.isimip.org/
140. Hugonnet, R. et al. Accelerated global glacier mass loss in the earlytwenty-first century. *Nature* **592**, 726–731 (2021).

Acknowledgements
We sincerely thank the Byrd Polar and Climate Research Center for providing the facilities and support essential for this research. We also express our gratitude to the three anonymous reviewers for their constructive comments and suggestions, which greatly improved the manuscript. We acknowledge CSR, JPL, and GSFC for providing the GRACE satellite data, and we are grateful to the ERA5 Land reanalysis project, ISIMIP future scenarios, IMERG, RGI, GLDAS, and NASA MODIS for making their datasets openly accessible.

Author contributions
J.K.D writing – original draft, Visualization, Software, Methodology, Formal analysis, Conceptualization. I.M.H. writing – review & editing, Supervision, Project administration, Funding acquisition, Conceptualization. A.P. writing – review & editing, Methodology, Formal analysis, Data curation, Visualization, Conceptualization.

Funding
This research has been supported by the Byrd Postdoctoral Fellowship awarded to JKD from the Byrd Polar and Climate Research Center, The Ohio State University.

Declarations

Competing interests
The authors declare no competing interests.

Additional information
Supplementary Information The online version contains supplementary material available at https://doi.org/10.1038/s41598-026-39404-8.

Correspondence and requests for materials should be addressed to J.K.D.

Reprints and permissions information is available at www.nature.com/reprints.

Publisher's note Springer Nature remains neutral with regard to jurisdictional claims in published maps and institutional affiliations.